Solution-Processed Parallel Tandem Polymer Solar Cells Using Silver Nanowires as Intermediate Electrode

Fei Guo,*,† Peter Kubis,† Ning Li,† Thomas Przybilla,‡ Gebhard Matt,† Tobias Stubhan,† Tayebeh Ameri,† Benjamin Butz,‡ Erdmann Spiecker,‡ Karen Forberich,† and Christoph J. Brabec*,†,§

†Institute of Materials for Electronics and Energy Technology (I-MEET), University of Erlangen-Nuremberg, Martensstrasse 7, 91058 Erlangen, Germany, ‡Center for Nanoanalysis and Electron Microscopy (CENEM), University of Erlangen-Nuremberg, Cauerstrasse 6, 91058 Erlangen, Germany, and §Bavarian Center for Applied Energy Research (ZAE Bayern), Haberstrasse 2a, 91058 Erlangen, Germany

ABSTRACT Tandem architecture is the most relevant concept to overcome the efficiency limit of single-junction photovoltaic solar cells. Series-connected tandem polymer solar cells (PSCs) have advanced rapidly during the past decade. In contrast, the development of parallel-connected tandem cells is lagging far behind due to the big challenge in establishing an efficient interlayer with high transparency and high in-plane conductivity. Here, we report all-solution fabrication of parallel tandem PSCs using silver nanowires as intermediate charge collecting electrode. Through a rational interface design, a robust interlayer is established, enabling the efficient extraction and transport of electrons from subcells. The resulting parallel tandem cells exhibit high fill factors of ~60% and enhanced current densities which are identical to the sum of the current densities of the subcells. These results suggest that solution-processed parallel tandem configuration provides an alternative avenue toward high performance photovoltaic devices.

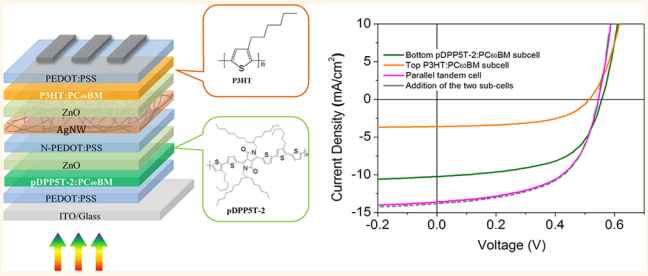

KEYWORDS: parallel-tandem · polymer solar cells · solution-processed · silver nanowires

The intense research interest in polymer solar cells (PSCs) stems from their promising potential in providing an affordable solar-to-electricity solution, which is primarily related to the low-cost materials and solution processability.[1,2] Over the past decade, the combination of photoactive material design, morphology control and interface engineering has led to a continuous increase in power conversion efficiency (PCE) of single junction PSCs from 2.5% to the level of 9%.[3−6] Despite these advances, the intrinsic drawbacks of low carrier mobility and spectrally limited absorption of organic semiconductors have suppressed further efficiency enhancement of the single junction devices.[7,8] In addition, one major deficiency associated with PSCs is the rather short exciton diffusion length (~10 nm) which also limits the thicknesses of the photoactive layer for photon harvest.[8] One effective strategy to circumvent these limitations and thereby improve the overall efficiency of PSCs is to make use of the tandem structure with complementary absorbers to harvest a larger spectral range of solar radiation.[9−11]

Two types of tandem configurations, series-connection and parallel-connection, which can also be termed as 2-terminal and 3-terminal,[10] are in principle capable of increasing the efficiency of PSCs by superimposing the photovoltage and photocurrent, respectively. Most efforts have so far been devoted to developing series-connected tandem PSCs with a considerable number of solution-processed charge recombination layers developed.[9−15] The stringent current-matching criterion of the series tandem devices requires a careful control of the respective active layer thickness to match number of photons absorbed in each subcell and thus balance the current generation. This generally results in the individual subcells having a layer thickness which does not correspond to the maximum efficiency in single junction devices. Consequently, high efficiency can only be

* Address correspondence to fei.guo@ww.uni-erlangen.de, christoph.brabec@ww.uni-erlangen.de.

Received for review September 30, 2014 and accepted November 18, 2014.

Published online November 18, 2014
10.1021/nn505559w

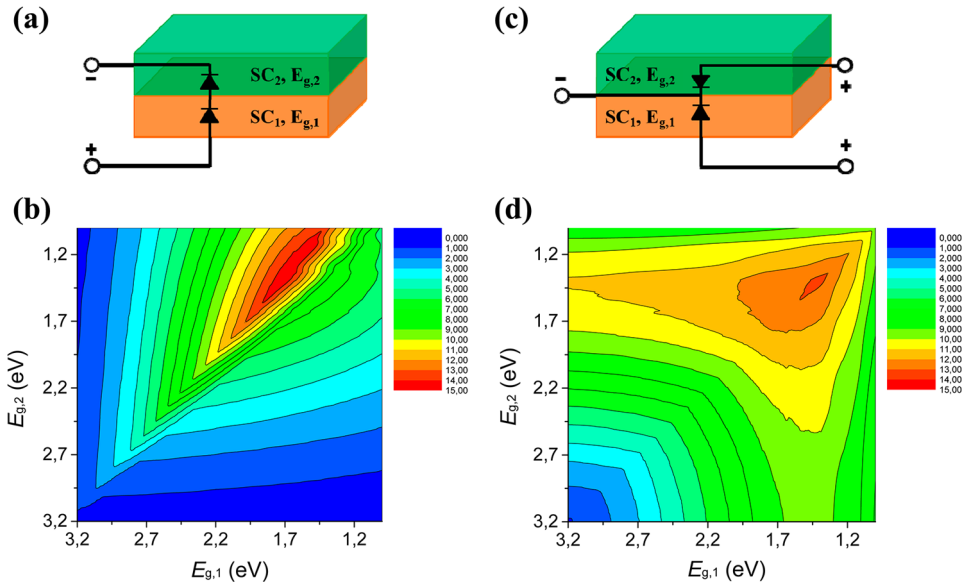

Figure 1. Comparison of the series-tandem and parallel-tandem polymer solar cells. (a) Schematic diagram of the series-connection and (b) the corresponding contour plot of the efficiency limits versus the bandgaps of semiconductors of the two subcells. (c) Schematic diagram of the parallel-connection and (d) the contour plot of the efficiency limits versus the bandgaps of semiconductors of the two subcells.

obtained with a very limited number of material combinations that have excellent complementary absorption.[14,15] On the other hand, the V_{oc} of organic solar cells is not as much sensitive to the bandgap of the absorber material as the V_{oc} of inorganic solar cells. This is due to the fact that the V_{oc} of the single junction PSCs is determined by the energy levels of the donors (conjugated polymers or small molecules) and acceptors (typically fullerene derivatives).[8,16] It is therefore possible to find absorbers with identical or similar V_{oc} and complementary absorption spectrum. Due to the absence of the current-matching criterion, the subcells of parallel tandem devices can be processed at their optimum thicknesses as in single junction cells.[17−25] Moreover, due to the thickness limitation of many high-performance polymers already mentioned above, the 3-terminal parallel tandem architecture provides a viable alternative for boosting the efficiency of PSCs by stacking two subcells of the same material.

To date, however, very few studies have been reported on parallel tandem PSCs primarily due to the challenge in introducing a solution-processed interconnecting electrode with high transparency and low sheet resistance. Carbon nanotubes,[20] graphene[21] and thermally deposited thin metal films[22−25] (e.g., Ag and Au) have been used as intermediate electrodes for the construction of parallel-tandem PSCs. However, these devices suffered from low fill factor (FF) and short-circuit current density (J_{sc}) due to the poor optoelectronic properties of the middle electrodes. For instance, the high sheet resistance of ∼500−700 Ω/sq of carbon-based films (carbon nanotubes and graphene) adversely increased the series resistance of the devices.[20,21] The low transmission (∼30−50% in the visible range) of the evaporated thin metal films (∼10−15 nm) caused a large optical loss for the back subcell.[22−25] Moreover, the involved transfer procedure and thermal vacuum deposition of the middle electrode increased the complexity in device fabrication which is incompatible with high volume roll-to-roll manufacturing processes.

In this work, we report a technically viable and scalable process for all-solution fabrication of monolithic parallel tandem PSCs using silver nanowires (AgNWs) as middle charge collecting electrode. We first performed optical simulations to show that parallel-tandem PSCs are capable of achieving efficiencies closing to the series-connected counterparts over a much wider choice of photoactive material combinations. We then designed and constructed an efficient intermediate layer, based on which parallel-tandem devices using different photoactive polymers as two subcells were fabricated by solution processing. Due to the excellent functionality of the intermediate layer, the as-prepared parallel tandem solar cells showed high FF of ∼60%. Significantly, the short-circuit current density of the parallel tandem cell is nearly identical to the sum of the current densities of the two subcells, indicating negligible resistance loss within the parallel connection. In addition, our solution-processed parallel tandem devices possess an impressive long-term stability when stored in ambient air without encapsulation.

RESULTS AND DISCUSSION

Optical simulations were first performed to compare the efficiency potential of the two tandem configurations. We followed the model proposed by Dennler et al. which had been used to calculate the efficiency limits of series-connected tandem PSCs (Figure 1a).[26]

For parallel tandem configuration (Figure 1c), we assumed $J_{sc,tan} = J_{sc,1} + J_{sc,2}$ and $V_{oc,tan} = \min(V_{oc,1}, V_{oc,2})$. A constant EQE of 65% and IQE of 85% were used for the calculation of both device configurations. Detailed description of the calculations can be found in the Experimental Section. Parts b and d of Figure 1 show the predicted efficiencies of tandem PSCs as a function of bandgap energies (E_g) of the bottom and top subcells, respectively, for series and parallel connection. Comparing the two different connection possibilities, the series connection shows a maximum efficiency of 15% for the optimum combination of bandgaps, whereas the parallel connection shows a lower maximum efficiency of 13.2%. However, it is also obvious that the parallel connection allows to have high efficiencies for a wider range of bandgap combinations. In addition, it should be noted that, owing to the thickness limitation of many conjugated polymers, the series-connected tandem cells often cannot reach the efficiency values predicted based on the bandgaps.[27] Therefore, the parallel connection can provide a more feasible alternative to reach high efficiencies with existing materials.

Similar to series tandem counterparts, the most crucial step for the successful fabrication of solution-processed parallel tandem PSCs is to develop an efficient and robust intermediate layer. The intermediate layer in parallel tandem devices generally contains a transparent electrode sandwiched between two interface layers with the same charge selectivity (n-type or p-type semiconductors). To achieve such an efficient interlayer with all layers solution-deposited, the selection of electrode material and the corresponding processing technique are of uttermost importance. First, the middle electrode should be highly conductive and transparent allowing lateral current flow and having minimal light absorption. Second, the solution processing of the intermediate layers, particularly the middle electrode, should not compromise the established underlying subcell and be robust enough as a mechanical foundation withstanding the solution-deposition of top subcell. In addition, a low surface roughness of the solution-processed interlayer is desirable to avoid shunting or short-circuiting the top subcells.

Following these guidelines, we chose AgNWs as the middle charge-collecting electrode because of their outstanding optoelectronic properties (transmittance ~90% at 550 nm with sheet resistance $\approx 10\Omega$ sq^{-1}) and solution processability with various coating methods.[28−31] We designed and fabricated the intermediate layer with a layer sequence of zinc oxide nanoparticles (ZnO)/neutral PEDOT:PSS/AgNW/ZnO. In this intermediate layer, ZnO was chosen as electron-extraction material due to its high electron mobility and the good match of the work function with the acceptors. We additionally introduced a layer of the polymer PEDOT:PSS which exclusively serves as a pinhole-free protective layer to avoid damaging the underlying active layer by solvent infiltration during the top active layer deposition. ZnO nanoparticle films are known to be readily dissolved in acidic media and therefore a neutral PEDOT:PSS (N-PEDOT) is chosen to be coated on top of the ZnO layer.[32,33] It was observed that the introduction of the neutral PEDOT:PSS between the ZnO and AgNWs showed no negative effect on device performance due to the formation of quasi ohmic contacts at the interface between ZnO and N-PEDOT as well as between N-PEDOT and AgNWs.[12,33] It is also worth mentioning that all the component interconnection layers was processed at reasonably low temperatures of <50 °C, and no high temperature annealing process is involved during device fabrication.

To examine the reliability of the interlayers, we first constructed and characterized a complete bottom subcell with a solution-processed AgNW top electrode, ITO/PEDOT:PSS/pDPP5T-2:PC_{60}BM/ZnO/N-PEDOT/AgNW, where pDPP5T-2 is a diketopyrrolopyrrole (DPP)-based low bandgap polymer (band gap: 1.41 eV).[13] Due to the lack of a reflective back electrode, the as-fabricated semitransparent device yields a photocurrent density of 8.13 mA cm^{-2} which is about 3 mA cm^{-2} lower than the reference with an evaporated Ag top electrode (Figure S1, Supporting Information). Importantly, comparable V_{oc} and FF values suggest that the solution-deposition of the AgNW electrode shows no negative effect on device performance. To test the solvent resistance, two commonly used organic solvents with high boiling point, chlorobenzene and *o*-dichlorobenzene, were bladed on top of the semitransparent devices. The current density−voltage ($J-V$) characteristics of the devices before and after solvent rinsing were compared. As shown in Figure S2 (Supporting Information), there are almost no changes in device performance in terms of V_{oc}, FF, and J_{sc}, suggesting that the as-fabricated interlayers is physically robust to protect the established bottom subcell from slow-drying solvents. In combination with our previous work on AgNWs as bottom electrode for inverted PSCs,[31] the as-designed intermediate layers is expected to effectively extract electrons from both bottom and top subcells.

Having achieved a robust interlayer with integration of a highly conductive and transparent AgNW electrode, we now complete the fabrication of the entire parallel tandem PSCs. The architecture of the parallel tandem devices is schematically shown in Figure 2a, where a bottom subcell with a normal structure and a top inverted cell are electrically connected in parallel. Accordingly, the middle AgNW electrode serves as a common cathode to collect electrons generated by the two subcells whereas the holes are collected by the connected bottom ITO and top Ag anodes. In this tandem device, other than the top Ag electrode which was deposited using vacuum thermal evaporation, the underlying 8 layers were sequentially doctor-bladed

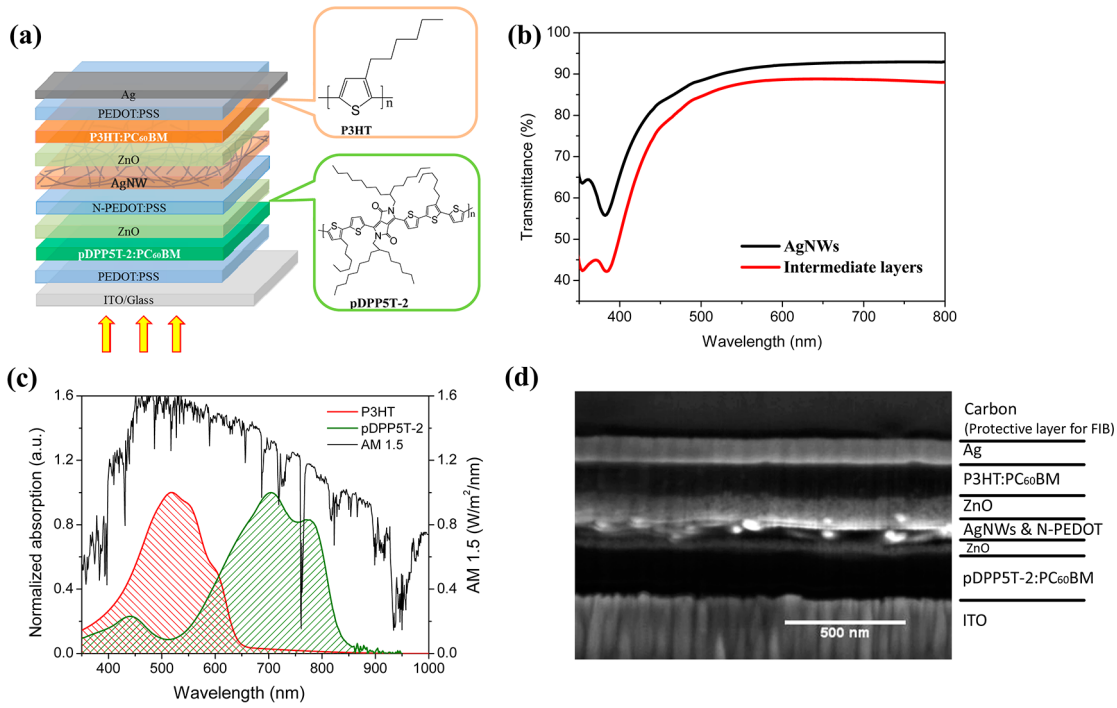

Figure 2. (a) Schematic architecture of the solution-processed parallel tandem cell and chemical structures of the two photoactive absorbers (P3HT and pDPP5T-2). (b) Transmittance of the AgNWs film and the intermediate layers consisting of "ZnO/N-PEDOT/AgNW/ZnO". Both films were prepared on glass substrates by doctor blading using the same coating parameters as in the tandem devices and measured against the glass substrate. (c) UV−vis absorption spectra of pDPP5T-2 and P3HT films and the AM 1.5G solar radiation spectrum. (d) Cross-sectional SEM image of a complete parallel tandem device. Note that the PEDOT:PSS layers between the ITO and bottom active layer and between the top active layer and the thermal deposited Ag cannot be distinguished in the SEM image.

on ITO-coated glass in ambient air. A detailed description of the device fabrication procedure is presented in the Experimental Section. We note that, to avoid a possible connection of the AgNWs with either the bottom ITO or top Ag electrode which may short-circuit the devices, the middle AgNW electrode was deposited in a confined area using a modified doctor-blading technique (as illustrated in Figure S3, Supporting Information). Figure 2b shows the transmittance spectra of the AgNWs film and the constructed intermediate layers consisting of "ZnO/N-PEDOT/AgNW/ZnO". The average transmittance (between 400 and 800 nm) of the AgNWs and the intermediate layers is 89.3% and 84.9%, respectively, which is much higher than evaporated semitransparent thin metal films (~30% - 50%).[22−25] This characteristic of the intermediate layers is highly favorable for tandem devices as it allows minimal absorption losses and high transmittance to the rear subcell of the tandem devices.

It is well-known that manufacturing of any kind of parallel tandem batteries requires the "voltage-matching criteria" and therefore a similar or identical voltage should be provided by the subcells. Here, pDPP5T-2 and P3HT were chosen as the two photoactive absorbers for our parallel tandem cells, because a similar V_{oc} can be achieved when they are blended with the acceptor $PC_{60}BM$. In addition, it can be seen from Figure 2c that the absorption profile of the P3HT perfectly fills the valley of the pDPP5T-2 spectrum, resulting in a broad combined absorption covering the solar spectrum from 350 to 850 nm. The excellent complementary absorption of the two materials makes them an appropriate combination for the construction of tandem solar cells. To minimize thermalization losses, polymer tandem cells generally use a large bandgap material as the front absorber to harvest high-energy photons and a small bandgap absorber as the back layer to absorb low-energy photons.[9,14,26] It should be noted that, however, the performance of parallel tandem solar cells is to a large degree determined by the sum photocurrent contributed by the subcells, provided that the subcells possess identical V_{oc} and FF values. In our parallel tandem situations, optical simulations shown in Figure S4 (Supporting Information) suggest that comparable efficiency can be achieved independent of the photoactive layers' sequence. From a practical point of view, however, a poor device performance of P3HT:$PC_{60}BM$ cell was observed when ZnO was coated on top of P3HT:$PC_{60}BM$ (Figure S5, Supporting Information), which is probably due to fact that the crystallization of P3HT changes the morphology of the upper ZnO film and other top layers.[34] We have thus employed pDPP5T-2:$PC_{60}BM$ as bottom absorber and P3HT:$PC_{60}BM$ as top photoactive layer for fabricating parallel-tandem solar cells.

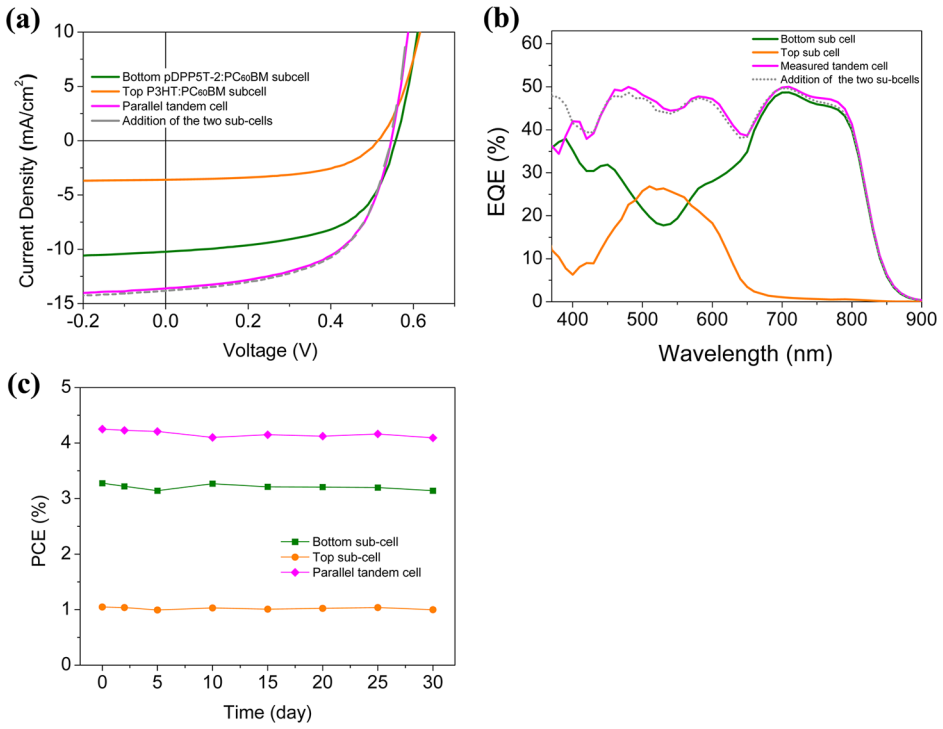

Figure 3. *J*–*V* characteristics (a) and the EQE spectra (b) of a typical parallel tandem device and the incorporated two subcells (pDPP5T-2:$PC_{60}BM$ and P3HT:$PC_{60}BM$). The gray dashed lines in (a) and (b) represent the mathematically added curves of the measured *J*–*V* and EQE characteristics of the two subcells, respectively. (c) Air stability of a parallel tandem cell and the two subcells which was stored and measured in ambient atmosphere.

A cross-sectional scanning electron microscopy (SEM) image of a complete parallel tandem solar cell is shown in Figure 2d. The cross-section was prepared using a focused ion beam (FIB, FEI Helios NanoLab 660) and subsequently imaged with the electron beam of the same instrument. Apart from the two interfaces between the photoactive layers and PEDOT:PSS which could not be distinguished due to the similiar contrast of the two organic materials, all the stacked layers and interfaces are clearly revealed in the scanning electron micrograph. We note that even though there is slight interlayer mixing between the AgNWs and the underlying N-PEDOT,[35] this interlayer mixing does not negatively affect the device functionality as the N-PEDOT in the intermediate layers solely functioned as "solvent protection" layer. Energy dispersive X-ray spectroscopy (EDS) mapping of the cross-section shown in Figure S6 (Supporting Information) confirmed the intermediate layers' organization. In particular, the sandwich status of the AgNWs between the two ZnO layers is clearly evidenced, which anticipates the full device performance for this sophisticated architecture, without artifacts from shunting or surface recombination.

An appealing feature of the parallel tandem configuration is the accessibility of the middle electrode which allows us to evaluate the photovoltaic behaviors of the two subcells in a straightforward manner. With a careful device layout design (Figure S7, Supporting Information), we are able to characterize

TABLE 1. Summary of Photovoltaic Parameters of the Studied Parallel Tandem Device (P3HT:pDPP5T-2) and the Incorporated Two Subcells

devices	J_{sc} (mA/cm^2)	V_{oc} (mV)	FF (%)	PCE (%)	R_p (kΩ cm^2)	R_s (Ω cm^2)
bottom subcell	10.22 (10.05)[a]	551	59.1	3.28	1.86	1.98
top subcell	3.60 (3.12)[a]	515	56.2	1.04	1.45	0.62
parallel tandem	13.58 (13.23)[a]	538	57.9	4.25	2.77	0.38

[a] J_{sc} values were calculated by integrating the EQE spectrum with the AM 1.5G spectrum.

the photoelectronic properties of the parallel tandem cell as well as of the two constituent subcells. Figure 3a shows the *J*–*V* characteristics of a typical parallel tandem device and the two subcells, measured under simulated AM 1.5G, 100 mW cm^{-2} illumination. The key performance parameters of the studied devices are summarized in Table 1. The parallel tandem solar cell exhibited a J_{sc} of 13.58 mA cm^{-2}, a V_{oc} of 540 mV, a FF of 58%, and a PCE of 4.25%. Significantly, we note that the measured J_{sc} value of 13.58 mA/cm^2 of the parallel tandem device is almost equal to the sum of the current densities of the two subcells, with 10.22 mA/cm^2 and 3.66 mA/cm^2 contributed by the front pDPP5T-2:$PC_{60}BM$ and back P3HT:$PC_{60}BM$ subcells, respectively. In particular, if we mathematically add the current density values of the two subcells at each operating voltage (Figure 3a), a good fitting of the resultant *J*–*V* curve with the measured tandem curve was observed, which is perfectly consistent with Kirchhoff's law. These

observations provide evidence that the two subcells have been efficiently connected in parallel.

External quantum efficiency (EQE) measurements were performed to investigate the spectral response of the parallel tandem device as well as the incorporated two subcells. As shown in Figure 3b, two complementary EQE curves of the two subcells, corresponding to the absorption spectra of the two absorber layers, and a flat EQE spectrum ranging from 400−800 nm for the parallel-connected device were observed. Integration of the EQE spectrum of the tandem cell with the AM 1.5G solar photon flux yields a current density of 13.23 mA cm^{-2}, which is quite close to the measured J_{sc} value of 13.58 mA cm^{-2}. The discrepancy of <3% indicates that the mismatch between simulated sunlight and the standard AM 1.5G is negligibly small. Significantly, an excellent spectral agreement between the measured EQE curve of the tandem device ($J_{sc,parallel}$ = 13.23 mA cm^{-2}) and the mechanically added EQE curves of the two subcells ($J_{sc,bottom}$ = 10.05 mA cm^{-2}, $J_{sc,top}$ = 3.12 mA cm^{-2}) was demonstrated (Figure 3b). This observation strongly supports the conclusion that the charge carries which were extracted by the subcells can also be efficiently collected and transported by the middle electrode in the parallel-connected state. Combined with the observed high FF (56%−59%) of the two subcells and the parallel tandem cell, these results suggest that the established intermediate layers are highly efficient for the extraction and transport of charge carriers, without significant recombination and resistance losses.

In order to obtain a straightforward comparison between the two types of tandem configurations, we simultaneously fabricated series-connected tandem solar cells using the same materials combination of pDPP5T-2 and P3HT. As indicated by optical simulations shown in Figure S8 (Supporting Information), higher efficiency can be obtained when P3HT:$PC_{60}BM$ is employed as the absorber of the bottom subcell. Inverted series-tandem devices with P3HT:$PC_{60}BM$ as bottom active layer and pDPP5T-2:$PC_{60}BM$ as top absorber were thus constructed. $J-V$ curves and the corresponding performance parameters of the two reference cells as well as the typical parallel-connected and series-connected tandem cells are presented in Figure S9 and Table S1 (Supporting Information), respectively. The series-connected tandem cell showed a J_{sc} = 5.83 mA/cm^2, FF = 58.3%, and V_{oc} = 1100 mV, yielding a PCE of 3.73% which is ~0.5% lower than the parallel-connected counterpart. The relatively low efficiency of the series-tandem cell was mainly due to the low current-density of the devices which was limited by low current of the bottom P3HT:$PC_{60}BM$ subcell. Based on these experimental results and optical simulations, we anticipate that parallel tandem configuration potentially offers a solution to lift the thickness limitation of many high-performance semiconductors in single junction cells.

We have also tested the air stability of the constructed parallel tandem solar cells. The devices were stored and measured in ambient atmosphere without any kind of encapsulation. The $J-V$ curves of a parallel tandem cell as well as the incorporated two subcells were regularly tested during the lifetime characterization. As shown in Figure 3c, an excellent long-term stability was observed: the parallel-tandem as well as the two subcells maintained more than 95% of their initial PCE after a period of 30 days. Remarkably, we have found almost no drops in short-circuit photocurrent (Figure S10, Supporting Information), indicating negligible photodegradation within the two absorber layers and sufficient robustness of the intermediate layers. The almost constant PCE of the parallel tandem device can therefore be attributed to a combined effect of the slightly enhanced V_{oc} and decreased FF of the two subcells (Figure S10, Supporting Information). We note that the decrease in FF can be mainly attributed to the increased series resistance of the devices as suggested by dark $J-V$ characteristics (Figure S11, Supporting Information). We ascribe the long-term stability of the parallel tandem devices to the stable PEDOT:PSS layer and the high work function Ag electrode as well as the interface between them. These layers in inverted organic solar cells can act as compact barriers to effectively prevent oxygen and water from entering the active layers.[36]

In the end, to verify the versatility of the solution-processed intermediate layers we further evaluate the general applicability of the parallel tandem architecture to other material combinations, pDPP5T-2:pDPP5T-2 and pDPP5T-2:GEN-2.[27] The measured $J-V$ characteristics and EQE curves are presented in Figure 4, with key device performance parameters summarized in Table S2 (Supporting Information). When pDPP5T-2 was used for both the bottom and top subcell (Figure 4a and 4b), a high J_{sc} value of 13.7 mA/cm^2 was obtained for the parallel tandem cell which is 2.7 mA/cm^2 higher than the single-junction reference device. The increased photocurrent in combination with well-maintained FF of the tandem device resulted in an increased PCE of 4.20%. If we compared the EQE curve of the parallel tandem cell (Figure 4b) to the EQE curve of the single-junction pDPP5T-2:$PC_{60}BM$ reference (Figure S9b, Supporting Information), one can see that the improved J_{sc} value mainly comes from the increased photoresponse at the lowest absorption region of the pDPP5T-2 between 450 and 700 nm. In the case of the system of pDPP5T-2:$PC_{60}BM$ and GEN-2:$PC_{60}BM$ where the two subcells possess different V_{oc} values (Figure 4c), the V_{oc} (558 mV) of the resulting parallel tandem cell was observed to be close to the V_{oc} value (541 mV) of the pDPP5T-2:$PC_{60}BM$ subcell. This is mainly due to the higher charge carrier injection of the pDPP5T-2:$PC_{60}BM$ subcell than the GEN-2:$PC_{60}BM$ subcell at forward bias. Again, for both material

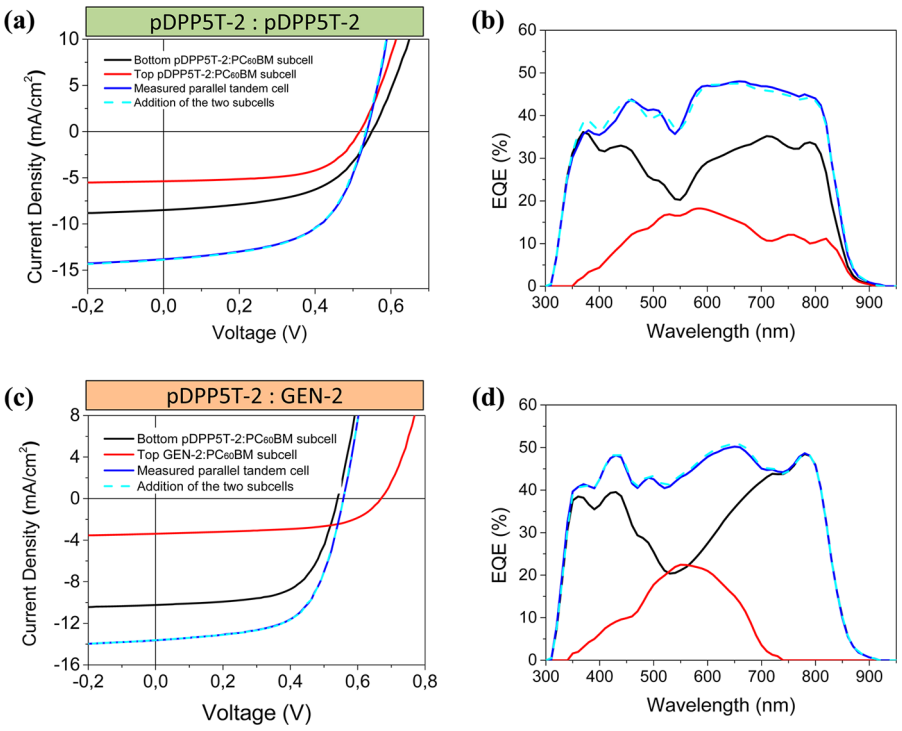

Figure 4. *J*–*V* (a) and EQE (b) curves of the parallel tandem PSCs using the pDPP5T-2:$PC_{60}BM$ as both the bottom and top subcells. (c, d) *J*–*V* and EQE curves of the parallel tandem device using the pDPP5T-2 and GEN-2 as the bottom and top subcells, respectively.

combinations the numerical addition of the J-V curves and EQE curves of the subcells fits perfectly to the corresponding measurements of the parallel tandem devices, indicating no significant resistance and recombination losses of the parallel connections. These results confirm the general applicability of the solution-processed parallel geometry to many different donor materials.

CONCLUSIONS

In summary, we demonstrated for the first time, a general approach for all-solution fabrication of parallel tandem polymer solar cells. The established robust and efficient intermediate layer incorporating a AgNW network allows efficient charge extraction and light transmission. The resulting parallel-tandem devices showed high FFs of ~60% and enhanced photocurrent values which are identical to the sum value of the two subcells, without any losses. Our theoretical and experimental results suggest that parallel tandem geometry holds great potential to boost the efficiencies of the photovoltaic devices. Based on the easy processing and general application of the intermediate layer, we expect that significant enhancement of efficiency can be achieved by employing high-performance photoactive materials.

EXPERIMENTAL SECTION

Materials and Device Fabrication. On laser patterned ITO substrates with a sheet resistance of 15 Ω sq^{-1}, parallel tandem PSCs with a layer stack shown in Figure 2a were solution-processed layer-by-layer using doctor-blading under ambient conditions. Specifically, PEDOT:PSS (Clevious P VP Al 4083, 1:3 vol % diluted in isopropyl alcohol (IPA)) was first bladed on precleaned ITO substrate and annealed at 140 °C for 5 min to obtain a layer thickness of ~40 nm. On top of the PEDOT:PSS, the bottom photoactive blend consisting of pDPP5T-2 (batch: GKS1–001, M_w = 47000 g mol^{-1}, PDI = 2.2) and $PC_{60}BM$ with 1:2 ratio dissolved in a mixed solvent of 90% chloroform and 10% *o*-diclorobenzene was deposited at 45 °C to obtain the bottom active layer with a thickness of ~140 nm. The intermediate layers, ZnO (Nanograde AG, Product N-10)/N-PEDOT:PSS (Agfa, Orgacon NT5–2)/AgNW (Cambrios, ClearOhm Ink)/ZnO, were sequentially bladed from their original solutions and annealed at 100 °C for 5 min in air after each layer's deposition. The corresponding thickness of the intermediate layer is approximately 30 nm/20 nm/90 nm/100 nm, and the resulting AgNW electrode shows a sheet resistance of ~8 ohm/sq. Afterward, a blend of P3HT:$PC_{60}BM$ with thickness ~150 nm was deposited as the top photoactive layer. Finally, a thin layer (~15 nm) of PEDOT:PSS (1:5 vol % diluted in IPA) was doctor-bladed serving as electron blocking layer. With all the solution-processed layers completed, Q-tips dipped with toluene were used to clean the edges of the substrate to expose the bottom ITO and middle AgNW contacts. Before vacuum deposition of the top Ag electrode, the whole stack was annealed in a N_2-filled glovebox at 140 °C for 5 min to crystallize the P3HT. To complete the device fabrication, a 100 nm thick Ag layer was thermally evaporated on top of PEDOT:PSS through a shadow mask to define the active area of the devices (~2 × 5.2 mm^2). To achieve a reliable contact between the middle AgNW electrode and the probes of the measurement setups (J-V and EQE measurements), silver paste or evaporated silver was applied to the exposed AgNWs (Figure S7b, Supporting Information).

Parallel-tandem devices with materials combination of pDPP5T-2:pDPP5T-2 and pDPP5T-2:GEN-2 were fabricated in a similar way as the pDPP5T-2:P3HT tandem devices. To achieve a better charge selectivity for the top inverted pDPP5T-2 and GEN-2 subcells, thermally evaporated MoO_x/Ag (10 nm/100 nm) was used as top electrode. Series-connected tandem solar cells with a device structure of "ITO/ZnO/P3HT:PC_{60}BM/PEDOT:PSS/ZnO/pDPP5T-2: PC_{60}BM/MoO_x/Ag" were simultaneously fabricated. Detailed processing procedure of this inverted structure tandem PSCs can be found in our previous work.[13] Here, following the simulations shown in Figure S8 (Supporting Information), a variation of the thicknesses of the two active layers was carried out to match the current flow. As a result, a ~120 nm-thick P3HT:PC_{60}BM and ~150 nm pDPP5T-2:PC_{60}BM was chosen due to the high FF and PCE that can be achieved for these series-connected tandem cells.

Device Characterization. *J*−*V* characteristics of all the devices were measured using a source measurement unit from BoTest. Illumination was provided by a Newport Sol1A solar simulator with AM 1.5G spectrum and light intensity of 100 mW cm^{-2}, which was determined by a calibrated crystalline Si-cell. The EQE spectra were measured with a home-built setup using Varian CARY 500 Scan spectrometer with a tungsten light source and a lock-in amplifier. During *J*−*V* and EQE recordings, a shadow mask with a single aperture (1.5 × 3 mm^2) which is smaller than the active area was used to obtain reliable photocurrent density values. The parallel tandem device pDPP5T-2/P3HT was unpacked and kept in dark during the stability measurement.

Optical Simulations. We followed the model proposed by Dennler et al. to calculate the efficiency limits of the two tandem PSCs configurations.[26] Basic assumptions are as follows:

EQE = 0.65 (for single junction cell with reflective back electrode)

IQE = 0.85 (both EQE and IQE are assumed to be constant in the entire absorption range)

FF = 0.65

$$V_{oc} = \frac{1}{e}(E_g - 0.6\ \text{eV}) \quad (\text{ref } 37)$$

LossMirror = 0.15 (accounts for the absorption losses of the first subcells due to the lack of back reflective electrode)

EQE_1 = EQE*(1 − LossMirror) (indicates the EQE of the front subcell)

EQE_2 = (1 − EQE_1/IQE)*EQE (indicates the EQE of the back subcell)

J_{sc} is calculated by integrating the EQE with solar spectrum AM1.5 G with intensity of 100 mA/cm^2

$$J_{sc} = \frac{q}{hc}\int_{\lambda 1}^{\lambda 2} P_{\text{AM1.5G}}(\lambda) \times \lambda \text{EQE}(\lambda) \text{d}\lambda$$

where *h* is Planck's constant, *c* is the speed of light in vacuum, and λ_1 and λ_2 are the limit absorption spectrum of the active layer.

According to Kirchoff's circuit law, the V_{oc} and J_{sc} of the series or parallel tandem cells and their respective subcells should meet the following relationships.

For series connection:

$$V_{oc,\tan} = V_{oc,1} + V_{oc,2}$$

$$J_{sc,\tan} = \min[J_{sc,1}; J_{sc,2}]$$

For parallel connection:

$$V_{oc,\tan} = \min[V_{oc,1}; V_{oc,2}]$$

$$J_{sc,\tan} = J_{sc,1} + J_{sc,2}$$

Conflict of Interest: The authors declare no competing financial interest.

Supporting Information Available: *J*−*V* characteristics of pDPP5T-2:PC_{60}BM solar cells with top Ag and AgNWs electrodes, solvent resistance test of the intermediate layers, schematic illustration of the modified doctor-blade for the deposition of middle AgNW electrode, contour plots of the calculated PCE of parallel tandem devices using pDPP5T-2:PC_{60}BM and P3HT:PC_{60}BM as subcells, *J*−*V* curves of semitransparent P3HT:PC_{60}BM cells with AgNWs top electrode, EDS (Ag, Zn, In, Si) mapping of the cross-section of an as-fabricated parallel tandem device, three terminal layout design, contour plots of the calculated PCE of series-connected tandem devices using pDPP5T-2:PC_{60}BM and P3HT:PC_{60}BM as subcells, *J*−*V* and EQE characteristics of the reference devices and the series tandem solar cell, table of photovoltaic parameters of the reference devices and the two tandem PSCs, air stability of a parallel tandem device, logarithmic dark *J*−*V* characteristics of the parallel tandem solar cell, and table of photovoltaic parameters of the two parallel tandem PSCs with material combinations of pDPP5T-2:pDPP5T-2 and pDPP5T-2:GEN-2. This material is available free of charge *via* the Internet at http://pubs.acs.org.

Acknowledgment. This work was supported by the Cluster of Excellence "Engineering of Advanced Materials" (EAM) and the SFB 953 at the University of Erlangen-Nuremberg. K.F. gratefully acknowledges use of the services and facilities of the Energie Campus Nürnberg and financial support through the "Aufbruch Bayern" initiative of the state of Bavaria. T.P. acknowledges funding via the DFG research training group GRK 1896. F.G. would like to acknowledge the funding from the China Scholarship Council.

REFERENCES AND NOTES

1. Brabec, C. J.; Sariciftci, N. S.; Hummelen, J. C. Plastic Solar Cells. *Adv. Funct. Mater.* **2001**, *11*, 15–26.
2. Krebs, F. C. Fabrication and Processing of Polymer Solar Cells: A Review of Printing and Coating Techniques. *Sol. Ener. Mater. Sol. Cells* **2009**, *93*, 394–412.
3. Ma, W.; Yang, C.; Gong, X.; Lee, K.; Heeger, A. J. Thermally Stable, Efficient Polymer Solar Cells with Nanoscale Control of the Interpenetrating Network Morphology. *Adv. Funct. Mater.* **2005**, *15*, 1617–1622.
4. Graetzel, M.; Janssen, R. a. J.; Mitzi, D. B.; Sargent, E. H. Materials Interface Engineering for Solution-Processed Photovoltaics. *Nature* **2012**, *488*, 304–312.
5. Shaheen, S. E.; Brabec, C. J.; Sariciftci, N. S.; Padinger, F.; Fromherz, T.; Hummelen, J. C. 2.5% Efficient Organic Plastic Solar Cells. *Appl. Phys. Lett.* **2001**, *78*, 841–843.
6. He, Z.; Zhong, C.; Su, S.; Xu, M.; Wu, H.; Cao, Y. Enhanced Power-Conversion Efficiency in Polymer Solar Cells Using an Inverted Device Structure. *Nat. Photonics* **2012**, *6*, 593–597.
7. Kirchartz, T.; Taretto, K.; Rau, U. Efficiency Limits of Organic Bulk Heterojunction Solar Cells. *J. Phys. Chem. C* **2009**, *113*, 17958–17966.
8. Blom, P. W.; Mihailetchi, V. D.; Koster, L. J. A.; Markov, D. E. Device Physics of Polymer: Fullerene Bulk Heterojunction Solar Cells. *Adv. Mater.* **2007**, *19*, 1551–1566.
9. Kim, J. Y.; Lee, K.; Coates, N. E.; Moses, D.; Nguyen, T. Q.; Dante, M.; Heeger, A. J. Efficient Tandem Polymer Solar Cells Fabricated by All-Solution Processing. *Science* **2007**, *317*, 222–225.
10. Ameri, T.; Li, N.; Brabec, C. J. High Efficient Organic Tandem Solar Cells: Follow up Review. *Energy Environ. Sci.* **2013**, *6*, 2390–2413.
11. Li, W.; Furlan, A.; Hendriks, K. H.; Wienk, M. M.; Janssen, R. A. Efficient Tandem and Triple-Junction Polymer Solar Cells. *J. Am. Chem. Soc.* **2013**, *135*, 5529–5532.
12. Gevaerts, V. S.; Furlan, A.; Wienk, M. M.; Turbiez, M.; Janssen, R. A. Solution Processed Polymer Tandem Solar Cell Using Efficient Small and Wide bandgap Polymer: Fullerene Blends. *Adv. Mater.* **2012**, *24*, 2130–2134.
13. Li, N.; Baran, D.; Spyropoulos, G. D.; Zhang, H.; Berny, S.; Turbiez, M.; Ameri, T.; Krebs, F. C.; Brabec, C. J. Environmentally Printing Efficient Organic Tandem Solar Cells with High Fill Factors: A Guideline Towards 20% Power Conversion Efficiency. *Adv. Energy Mater.* **2014**, 10.1002/aenm.201400084.
14. Dou, L.; You, J.; Yang, J.; Chen, C. C.; He, Y.; Murase, S.; Yang, Y. Tandem Polymer Solar Cells Featuring a Spectrally

Matched Low-Bandgap Polymer. *Nat. Photonics* **2012**, *6*, 180–185.
15. You, J.; Dou, L.; Yoshimura, K.; Kato, T.; Ohya, K.; Moriarty, T.; Yang, Y. A polymer Tandem Solar Cell with 10.6% Power Conversion Efficiency. *Nat. Commun.* **2013**, *4*, 1446.
16. Brabec, C. J.; Cravino, A.; Meissner, D.; Sariciftci, N. S.; Fromherz, T.; Rispens, M. T.; Sanchez, L.; Hummelen, J. C. Origin of the Open Circuit Voltage of Plastic Solar Cells. *Adv. Funct. Mater.* **2001**, *11*, 374–380.
17. Shrotriya, V.; Wu, E. H.-E.; Li, G.; Yao, Y.; Yang, Y. Efficient Light Harvesting in Multiple-device Stacked Structure for Polymer Solar Cells. *Appl. Phys. Lett.* **2006**, *88*, 064104.
18. Hadipour, A.; De Boer, B.; Blom, P. W. M. Solution-Processed Organic Tandem Solar Cells with Embedded Optical Spacers. *J. Appl. Phys.* **2007**, *102*, 074506.
19. Hadipour, A.; De Boer, B.; Blom, P. W. M. Device Operation of Organic Tandem Solar Cells. *Org. Electron.* **2008**, *9*, 617–624.
20. Tanaka, S.; Mielczarek, K.; Ovalle-Robles, R.; Wang, B.; Hsu, D.; Zakhidov, A. A. Monolithic Parallel Tandem Organic Photovoltaic Cell with Transparent Carbon Nanotube Interlayer. *Appl. Phys. Lett.* **2009**, *94*, 113506.
21. Tong, S. W.; Wang, Y.; Zheng, Y.; Ng, M. F.; Loh, K. P. Graphene Intermediate Layer in Tandem Organic Photovoltaic Cells. *Adv. Funct. Mater.* **2011**, *21*, 4430–4435.
22. Sista, S.; Hong, Z.; Park, M. H.; Xu, Z.; Yang, Y. High-Efficiency Polymer Tandem Solar Cells with Three-Terminal Structure. *Adv. Mater.* **2010**, *22*, E77–E80.
23. Guo, X.; Liu, F.; Yue, W.; Xie, Z.; Geng, Y.; Wang, L. Efficient Tandem Polymer Photovoltaic Cells with Two Subcells in Parallel Connection. *Org. Electron.* **2009**, *10*, 1174–1177.
24. Zuo, L.; Chueh, C.-C.; Xu, Y.-X.; Chen, K.-S.; Zang, Y.; Li, C.-Z.; Chen, H.; Jen, A. K.-Y. Microcavity-Enhanced Light-Trapping for Highly Efficient Organic Parallel Tandem Solar Cells. *Adv. Mater.* **2014**, 10.1002/adma.201402782.
25. Tang, Z.; George, Z.; Ma, Z.; Bergqvist, J.; Tvingstedt, K.; Vandewal, K.; Wang, E.; Andersson, L. M.; Andersson, M. R.; Zhang, F.; Inganäs, O. Semi-Transparent Tandem Organic Solar Cells with 90% Internal Quantum Efficiency. *Adv. Energy Mater.* **2012**, *2*, 1467–1476.
26. Dennler, G.; Scharber, M. C.; Brabec, C. J. Polymer-Fullerene Bulk-Heterojunction Solar Cells. *Adv. Mater.* **2009**, *21*, 1323–1338.
27. Li, N.; Baran, D.; Forberich, K.; Machui, F.; Ameri, T.; Turbiez, M.; Carrasco-Orozco, M.; Drees, M.; Facchetti, A.; Krebs, F. C.; Brabec, C. J. Towards 15% Energy Conversion Efficiency: A Systematic Study of the Solution-processed Organic Tandem Solar Cells Based on Commercially Available Materials. *Energy Environ. Sci.* **2013**, *6*, 3407–3413.
28. Leem, D. S.; Edwards, A.; Faist, M.; Nelson, J.; Bradley, D. D.; de Mello, J. C. Efficient Organic Solar Cells with Solution-Processed Silver Nanowire Electrodes. *Adv. Mater.* **2011**, *23*, 4371–4375.
29. Kim, A.; Won, Y.; Woo, K.; Kim, C. H.; Moon, J. Highly Transparent Low Resistance ZnO/Ag Nanowire/ZnO Composite Electrode for Thin Film Solar Cells. *ACS Nano* **2013**, *7*, 1081–1091.
30. Guo, F.; Zhu, X.; Forberich, K.; Krantz, J.; Stubhan, T.; Salinas, M.; Halik, M.; Spallek, S.; Butz, B.; Spiecker, E.; *et al.* ITO-Free and Fully Solution-Processed Semitransparent Organic Solar Cells with High Fill Factors. *Adv. Energy Mater.* **2013**, *3*, 1062–1067.
31. Stubhan, T.; Krantz, J.; Li, N.; Guo, F.; Litzov, I.; Steidl, M.; Richter, M.; Matt, G. J.; Brabec, C. J. High Fill Factor Polymer Solar Cells Comprising a Transparent, Low Temperature Solution Processed Doped Metal Oxide/Metal Nanowire Composite Electrode. *Sol. Ener. Mater. Sol. Cells* **2012**, *107*, 248–251.
32. Gevaerts, V. S.; Furlan, A.; Wienk, M. M.; Turbiez, M.; Janssen, R. A. Solution Processed Polymer Tandem Solar Cell using Efficient Small and Wide Bandgap Polymer: Fullerene Blends. *Adv. Mater.* **2012**, *24*, 2130–2134.
33. Li, N.; Baran, D.; Forberich, K.; Turbiez, M.; Ameri, T.; Krebs, F. C.; Brabec, C. J. An Efficient Solution-Processed Intermediate Layer for Facilitating Fabrication of Organic Multi-Junction Solar Cells. *Adv. Energy Mater.* **2013**, *3*, 1597–1605.
34. van Franeker, J. J.; Voorthuijzen, W.; Gorter, H.; Hendriks, K. H.; Janssen, R. A.; Hadipour, A.; Andriessen, R.; Galagan, Y. All-solution-processed Organic Solar Cells with Conventional Architecture. *Sol. Ener. Mater. Sol. Cells* **2013**, *117*, 267–272.
35. Margulis, G. Y.; Christoforo, M. G.; Lam, D.; Beiley, Z. M.; Bowring, A. R.; Bailie, C. D.; Salleo, A.; McGehee, M. D. Spray Deposition of Silver Nanowire Electrodes for Semitransparent Solid-State Dye-Sensitized Solar Cells. *Adv. Energy Mater.* **2013**, *3*, 1657–1663.
36. Hau, S. K.; Yip, H. L.; Baek, N. S.; Zou, J.; O'Malley, K.; Jen, A. K. Y. Air-Stable Inverted Flexible Polymer Solar Cells Using Zinc Oxide Nanoparticles as an Electron Selective Layer. *Appl. Phys. Lett.* **2008**, *92*, 253301.
37. Veldman, D.; Meskers, S. C.; Janssen, R. A. The Energy of Charge-Transfer States in Electron Donor-Acceptor Blends: Insight into the Energy Losses in Organic Solar Cells. *Adv. Funct. Mater.* **2009**, *19*, 1939–1948.